

# Heterogeneity Spectrum of Earth's Upper Mantle Obtained from the Coherence of Teleseismic P Waves

Vernon F. Cormier<sup>1,\*</sup>, Yiteng Tian<sup>1</sup> and Yingcai Zheng<sup>2</sup>

<sup>1</sup> *Department of Physics, University of Connecticut, 2152 Hillside Road, Storrs, CT 06269, USA.*

<sup>2</sup> *Department of Earth and Atmospheric Sciences, University of Houston, 3507 Cullen Blvd, Houston, TX 77205, USA.*

Received 28 March 2018; Accepted (in revised version) 24 October 2018

---

**Abstract.** Fluctuations in log-amplitude and travel time of teleseismic P waves recorded by the EarthScope USArray are used to invert for the heterogeneity spectrum of P-wave velocity in a 1000 km thick region of the upper mantle beneath the array. These fluctuations are used to form coherence functions. Best fits to joint transverse coherence functions require a depth dependent heterogeneity spectrum, with peaks in narrow depth ranges. These peaks agree well with peaks predicted for the temperature derivative of seismic velocity from models of the chemistry and phase of silicate mineral assemblages appropriate for the upper mantle, correlating with the depths of phase changes. The results show that chemistry and phase act in concert with lateral and depth variations in temperature to produce the observed heterogeneity in seismic velocities in the upper mantle at spatial scales from 50 to 300 km.

**AMS subject classifications:** 86A15, 86A22, 74J20

**Key words:** Stochastic tomography, geophysical inversion.

---

## 1 Introduction

The chemistry, distribution, and shapes of small-scale heterogeneity record the history of compositional mixing of Earth's mantle by convection and plate tectonics. Directionally dependent scattering, focusing, and diffraction of seismic waves by small-scale heterogeneity also affects estimates of viscoelastic attenuation and anisotropy, which in turn are important for estimating temperature, mineral composition, and mineral phase. Travel-time tomography, however, fails to resolve heterogeneities having dimensions less than several dominant wavelengths of band-passed body waves. Resolvable scale lengths are

---

\*Corresponding author. *Email addresses:* [vernon.cormier@uconn.edu](mailto:vernon.cormier@uconn.edu) (V. F. Cormier), [yiteng.tian@uconn.edu](mailto:yiteng.tian@uconn.edu) (Y. Tian), [yzheng12@uh.edu](mailto:yzheng12@uh.edu) (Y. Zheng)

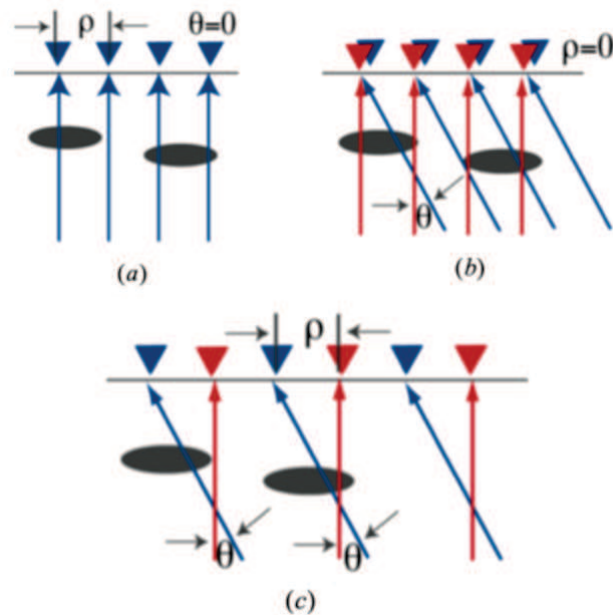


Figure 1: Teleseismic wave incidence on elements of receiver arrays (triangles) and their sensitivity to heterogeneity (gray ellipses) beneath the arrays determined from (a) Transverse Coherence Functions (TCF) [2], (b) angular coherence function (ACF) [3], and (c) joint transverse and angular coherence function (JTACF) [4, 5], where  $\theta$  denotes the incident angle between the two plane waves and  $\rho$  denotes the lag distance between receivers.

generally greater than 1,000 km from teleseismic body waves in the 0.01 to 0.2 Hz band. Tomographic imaging from higher frequency (1 Hz) body waves, recorded by dense regional arrays, occasionally is able to resolve structures smaller than several 100 kilometers, e.g., [1]. An alternative approach is to retrieve a statistical representation of structure from observations of the fluctuation of the amplitude and travel time of teleseismic body waves recorded by arrays. These fluctuations are created by small-scale heterogeneities beneath the arrays that scatter, focus, and defocus steeply incident body waves, which can be treated as plane waves incident on the upper mantle beneath the receivers. While deterministic seismic tomography gives both location, shape, and intensity of individual velocity heterogeneities, the stochastic approach provides an overall description about the assemblage of heterogeneities in terms of the spatial spectrum of velocity perturbations.

Aki [2] first proposed using the transverse coherence (Fig. 1a) of travel times and log amplitudes of teleseismic body waves to retrieve the heterogeneity spectrum of Earth structure beneath seismic arrays from steeply incident plane waves. Flatté and Wu [3] extended Aki's methods to include angular coherence (Fig. 1b), using seismic waves arriving from different incoming directions. Several studies by Wu and Flatté [4] and Chen and Aki [5] further extended this method to include observations of the joint transverse angular coherence (Fig. 1c). Wu and Xie [6] conducted successful inversions of joint

transverse angular coherence functions (JTACFs) measured from seismograms numerically synthesized in heterogeneous Earth models. They termed this method "stochastic tomography". Inversion of JTACFs are particularly effective in focusing sensitivity on narrow depth regions, where incident rays from plane waves arriving from different directions cross, allowing results to be obtained for scale lengths smaller than the array sensor spacing at the surface. These earlier works all assumed that the background medium is homogeneous. Zheng and Wu [7] extended stochastic tomography to allow a depth-dependent reference model of seismic velocity.

The study described in this paper applies stochastic tomography to derive a depth-dependent heterogeneity spectrum for the upper mantle beneath the USArray from observations of amplitude and phase coherences of teleseismic P waves. Section 2 describes the method of stochastic tomography; Section 3 describes our data and measurement of coherences; Section 4 summarizes the results of inversions for the heterogeneity spectrum for the upper 1000 km of mantle beneath the USArray; and Section 5 discusses the significance of the results for chemical and phase heterogeneity of the upper mantle. Measurement of coherences are described in greater detail in Appendix A. Appendix B described the approach we used for inverting for the heterogeneity spectrum from measured coherences.

## 2 Stochastic tomography

For a plane wave 1, we can measure the log amplitude  $u_1(r_1)$  and phase  $\phi_1(r_1)$  at a station  $r_1$ . Similarly, for a second plane wave 2, we can measure the log amplitude  $u_2(r_2)$  and  $\phi_2(r_2)$  at  $r_2$ . Using these measured quantities and equations from [7], we can form the following expressions for amplitude, phase, and amplitude/phase coherences:

$$\begin{aligned} \langle u_1 u_2 \rangle &= (2\pi)^{-1} \int_0^H d\xi a_1(\xi) a_2(\xi) \int_0^\infty J_0[\kappa R(\xi)] \cos[\omega\vartheta_1(\xi)] \cos[\omega\vartheta_2(\xi)] P(\xi, \kappa) \kappa d\kappa, \\ \langle \phi_1 \phi_2 \rangle &= (2\pi)^{-1} \int_0^H d\xi a_1(\xi) a_2(\xi) \int_0^\infty J_0[\kappa R(\xi)] \sin[\omega\vartheta_1(\xi)] \sin[\omega\vartheta_2(\xi)] P(\xi, \kappa) \kappa d\kappa, \\ \langle u_1 \phi_2 \rangle &= (2\pi)^{-1} \int_0^H d\xi a_1(\xi) a_2(\xi) \int_0^\infty J_0[\kappa R(\xi)] \sin[\omega\vartheta_1(\xi)] \cos[\omega\vartheta_2(\xi)] P(\xi, \kappa) \kappa d\kappa. \end{aligned} \quad (2.1)$$

In Eqs. (2.1),  $H$  is the thickness of the heterogeneous layer,  $\xi$  is depth,  $\kappa$  is the magnitude of the transverse wavenumber, which is the horizontal projection of the wavenumber vector.

The function  $a$  is given by:

$$a(p, \xi) = k^2(\xi) / k_z(p, \xi), \quad (2.2)$$

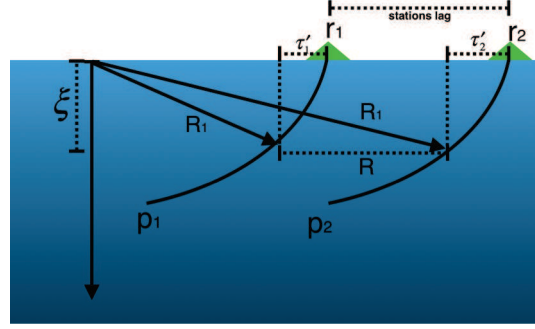


Figure 2: 2-D sketch of R function appearing in the argument of the Bessel function in Eq. (2.1).

where  $k(\xi) = \omega/c(\xi)$  is the background wavenumber at depth  $\xi$ ,  $k_z(p, \xi)$  the vertical wavenumber; and  $p$  the scalar ray parameter corresponding to the specific plane wave and  $c(\xi)$  is the reference velocity at depth  $\xi$ .

The function  $\vartheta$  is

$$\vartheta(p, \xi, \kappa) = \frac{1}{2} \frac{d^2 \tau}{dp^2} \frac{\kappa^2}{\omega^2}, \quad (2.3)$$

where

$$\tau(p, \xi) = \int_0^\xi dz \sqrt{c^{-2}(z) - p^2} \quad (2.4)$$

is the familiar delay or slope intercept time ( $\tau(p) - p\Delta(p)$ ).

The function  $R$  is

$$R(r_1, r_2, p_1, p_2, \xi) = \left| \vec{R}_1(p_1, \xi) - \vec{R}_2(p_2, \xi) \right|, \quad (2.5)$$

which is the horizontal distance of two rays at depth  $\xi$ , where  $\vec{R}_1(p_1, \xi)$  is the ray trajectory connecting station  $r_1$  for plane wave  $p_1$ , and  $\vec{R}_2(p_2, \xi)$  is the ray trajectory connecting station  $r_2$  for another plane wave  $p_2$ . The geometry in 2D is shown in Fig. 2, when the azimuths of two incoming waves are in the same direction with the station lag vector  $\vec{r}_1 r_2$ .

We use an autocorrelation function of the seismic P velocity of a heterogeneous medium to characterize the spatial scales of the magnitude of its irregularities. Here the function  $P(\xi, \kappa)$  is the Fourier transform of this autocorrelation function. It is also known as the power spectrum density function (PSDF) of the random medium.

A discretized version of Eq. (2.1) can be written as a product of a matrix and an unknown vector representing the medium power spectrum  $P(\xi, \kappa)$  discretized over intervals of depth  $\xi$  and transverse wavenumber  $\kappa$  (Appendix A). The unknown power spectrum can then be determined by linearized inversion (Appendix B) of the vector of observed coherences on the left hand side of a discretized version Eq. (2.1).

The assumptions used in the derivation of this theoretical coherence function are discussed and tested in previous work of Wu and Zheng, both theoretically [8, 9] and numerically [4, 6].

### 3 Data analysis

#### 3.1 Data selection and pre-processing

For data we used P waveforms recorded by all available stations in the USArray of the EarthScope project [10] in the western US between latitudes  $30^\circ$  N to  $50^\circ$  N, and longitudes  $100^\circ$  W to  $125^\circ$  W. Waveforms were selected from earthquakes in epicentral regions in the time range 2000-01-01 to 2017-10-01, available in Global Centroid Momentum Tensor (GCMT) catalog [11]. Events and stations are shown in Fig. 3. The grouping of waveforms and inversions into results for three broad epicentral regions follows a procedure similar to that used in a study by Zheng [12] to retrieve the heterogeneity spectrum beneath the Hi-Climb array in Tibet. Only deep focus earthquakes were chosen to minimize effects of heterogeneity in the upper mantle of the source region and to remove surface reflections and crustal interactions near the sources. Elimination of near source reflections improves the accuracy of the empirical source-time functions (Section 3.2) used in the constructing reference waveforms. The three epicenter regions chosen for analysis were:

1. Earthquakes from the Japan area: latitude from  $25^\circ$  N to  $35^\circ$  N, longitudes from  $135^\circ$  E to  $145^\circ$  E, depth from 400 km to 500 km, magnitude from 5.8 mw to 6.2 mw.
2. Earthquakes from the Tonga area: latitude from  $15^\circ$  S to  $30^\circ$  S, longitudes from  $175^\circ$  E to  $175^\circ$  W, depth from 500 km to 700 km, magnitude from 5.8 mw to 6.2 Mw.
3. Earthquakes from the Chile area: latitude from  $15^\circ$  S to  $30^\circ$  S, longitudes from  $100^\circ$  W to  $125^\circ$  W, depth from 500 km to 700 km, magnitude from 5.8 to 6.2 Mw.

In pre-processing of waveforms, we removed the instrument response and filtered the seismograms with a band pass window between 0.3 Hz to 1.5 Hz, and then selected only high signal to noise ratio (SNR) waveforms, using the classic calculation method [13] and a selection threshold of 6. About 40 percent of seismograms were usable under this criterion.

#### 3.2 Calculation of reference P waveforms in the reference model

Since  $u_1$  and  $u_2$  (or  $\phi_1, \phi_2$ ) are fluctuations of the amplitude or phase with respect to their background values in the reference model, waveforms synthesized in a reference Earth model are required. The 3-D tomographic images of P velocity that exist for our region of study reveal a rich spectrum of heterogeneity at scales of several hundred kilometers,

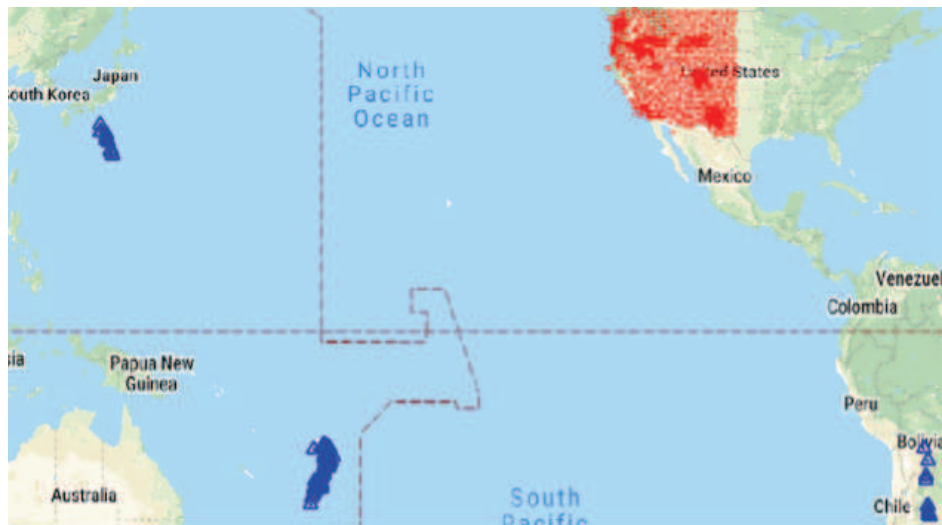


Figure 3: Epicenter groups (blue) and US transportable array elements (red) included in study.

affected by a complex tectonic history of subduction and hot-spot tracks, e.g. [14]. The velocity perturbations of these models are typically on the order of a 1%, too small to generate significant focusing, defocusing, and multi-pathing, consistent with the assumptions of linear tomography. Thus, even if forward modeling were numerically tractable, there is no advantage in assuming a fully 3-D reference model having this order of P velocity perturbation in an inversion that seeks to match the amplitude coherence of P waves. Hence, we have chosen a 1-D reference Earth model.

The P waves we studied are in an epicentral distance range ( $40^\circ$  to  $90^\circ$ ), removed from the range in which body waveforms are affected by triplicated interference from interaction with upper mantle phase changes. Although simple ray theory can be employed in this distance range to accurately model geometric spreading and travel time, we instead synthesized P waveforms using the 2.5D numerical code AxiSem [15,16] provided by the IRIS Syngine service [17]. We used the IASP91 model [18] as the reference Earth model. To use the IRIS Syngine service, earthquake moment tensors and source time functions must be supplied to represent the far-field earthquake sources. For moment tensors, we used the GCMT solutions Global Centroid-Moment-Tensor [11,19] included as raw metadata for each earthquake. Source-time functions were constructed empirically (Fig. 4) from P waves stacked for each source, avoiding stations on nodes of radiation patterns.

### 3.3 Measurement of coherences

For amplitude fluctuations, the measurement is straightforward. After Fourier transforming the time-domain waveform using a multi-taper method [20,21], the log amplitude is measured at frequency 0.7 Hz. For measuring the phase fluctuations, we used

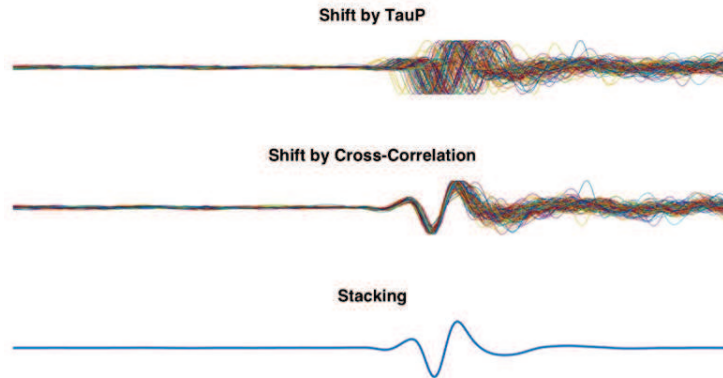


Figure 4: Procedure of aligning and stacking P waveforms used to retrieve the empirical source-time function.

a waveform cross-correlation method [22]. We first find the travel-time fluctuation and corresponding phase  $\delta\phi = \omega \cdot \delta t$ , and then shift the waveform to calculate the argument function of the waveform in frequency domain [8]. The final phase fluctuation is the sum of these two calculations. We also used the empirical source-time function to cross correlate all the waveforms twice for better precision. After applying this processing to both seismograms and reference synthetics, we subtracted observed amplitudes and travel times from those predicted by the reference Earth model to get fluctuations of log amplitude and phase.

The next step is to calculate the coherence functions using these fluctuations. For transverse coherence functions (TCFs), we care about the coherence over the lag distance between receivers. Therefore for every two fluctuation values at two stations (either log amplitude or phase), we calculate the respective station lag distance and round it to the nearest 10 km increment intervals, multiply the fluctuations as coherence, and take the statistical mean of all products from all station pairs at each 10 km interval. Since seismic waves from similar epicenter locations will result in the same TCFs, we can sum up the results associated with all seismic waves from nearby areas as an "earthquake group", assuming that they share the same event depth and location (longitude and latitude). This assumption means that events from the same earthquake group will share the same incidence angle beneath a receiver. We calculated all incident angles of source-receiver pairs, and performed a statistical study of the angle difference within the same earthquake group. We found that the average incident angle difference is around 1.1 degree, indicating a  $\pm 8$  km positioning error for a 1000 km thick layer, which is acceptable for the resolution for this study. By averaging the seismic waveforms, we reduce noise, similar to filtering data via stacking. The summation of earthquake waveforms from groups of events in a broad region will also tend to remove and smooth over any unhealed amplitude and phase fluctuations induced by heterogeneities in the upper mantle beneath the source region. After all these steps, the coherence functions are calculated for these three different earthquake groups.

In all coherence inversions we applied a “quasi-homogeneous” approximation [2], which is equivalent to assuming that the power spectrum  $P(z,k)$  is a 2-D function of depth and wavenumber. This ignores the possibility of anisotropy of heterogeneity scale lengths, which includes the case of horizontally or vertically stretched heterogeneities. Evidence of such scale-length heterogeneity in the crust and upper mantle has been found in the studies of travel-time covariances [23] and is well established in some tomographic images of the plate-decoupling region (the lithosphere/asthenosphere boundary), e.g., [24]. The near-vertical incidence of our teleseismic P data, however, does not span a sufficiently broad range of angles of incidence to resolve any anisotropy of heterogeneity scale lengths.

We investigated, but dismissed, the use of joint transverse angular coherence functions (JTACFs) to describe the cross coherence of different events at different receivers. In this case, the inverse problem becomes 10-D, depending on two receiver locations and two source locations (latitudes, longitudes; or equivalently incident angle, azimuth, and lag distance). Applying a quasi-homogeneous approximation, the problem is reduced to 6-D but is still too high in dimension for practical inversion. An inversion of JTACFs would also require a much broader range of incidence angles than is possible with our data. Furthermore, the irregular distribution of event locations makes it also almost impossible to form a generalized mapping from the power spectrum to the coherence functions without further approximations.

## 4 Inversion results

### 4.1 Single layer with an L-2 norm

In this case, we assume that the power spectrum is independent of depth in a 1000 km thick layer beneath the receiver array. We construct an object function to minimize of the form

$$\min \left( \|M_t P_{mn} - C_{ij}\|^2 + \lambda L P_{mn} \right) \quad (4.1)$$

(see Appendix B for the definition of the symbols in Eq. (4.1)). The second term of Eq. (4.1) is an L-2 Tikhonov regularization [25], where L is first order derivative operator matrix and  $\lambda$  is a small real number that can be determined by the L-curve technique. The result is shown in Fig. 5. A comparison of the best fit to observed coherence functions predicted from the inverted power spectrum is shown in Fig. 6.

For this model, the R-squared (coefficient of determination) is 0.74 and the reduced chi-squared is 1.65. The reduced chi-squared is calculated as chi-squared per degree of freedom, as an indicator of goodness of fit. If the value is above 1, it means the problem is under-fit. If the value is below 1, it means too many pending parameters are chosen, resulting in an over-fit.

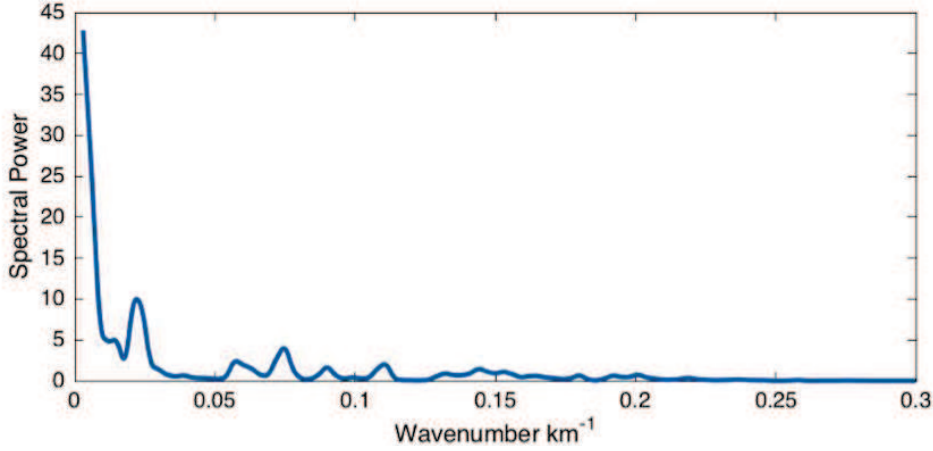


Figure 5: Inversion result: spectrum retrieved under a single layer approximation and L-2 regularization.

#### 4.2 Inversion regularized by a parameterization of spectrum function

Klimes [26] demonstrated that most of the commonly studied random media are special cases of the following function:

$$\hat{F}(k) = \sigma^2 [a_v^{-2} + k^2]^{-\frac{d+2N}{2}} \exp\left(-\frac{a_g^2 k^2}{4}\right), \quad (4.2)$$

where  $d$  is the spatial dimension,  $k$  is the wavenumber,  $\sigma$  is the parameter of model variance, and  $N$  is defined as the Hurst parameter.  $a_g$  and  $a_v$  are the correlation lengths, which are the Gaussian correlation length and von Karman correlation length respectively.

Using this equation, the shape of the power spectrum in wavenumber  $k$  can be written as a function of 4 unknown parameters  $a_g, a_v, \sigma, N$ . The object function then becomes

$$\min\left(\|M_t P(a_v, a_g, \sigma, N) - C_{ij}\|^2\right). \quad (4.3)$$

Using a constraint on the Hurst parameter, for physically reasonable scaling properties of geological structures [27, 28]:

$$-\frac{3}{2} \leq N \leq 1. \quad (4.4)$$

Recognizing that  $P(a_v, a_g, \sigma, N)$  is a nonlinear function, an iterative solution using a gradient descent is used to locate the parameters that minimize Eq. (4.3). With  $X$  standing for one parameter of  $(a_v, a_g, \sigma, N)$ , we have

$$X_{new} = X_{old} - \gamma \cdot \nabla \|M_t P(X_{old}) - C_{ij}\|, \quad (4.5)$$

which is

$$X_{new} = X_{old} - \gamma \left( M_t^T (M_t P(X_{old}) - C_{ij}) \right)^T J_{PX}, \quad (4.6)$$

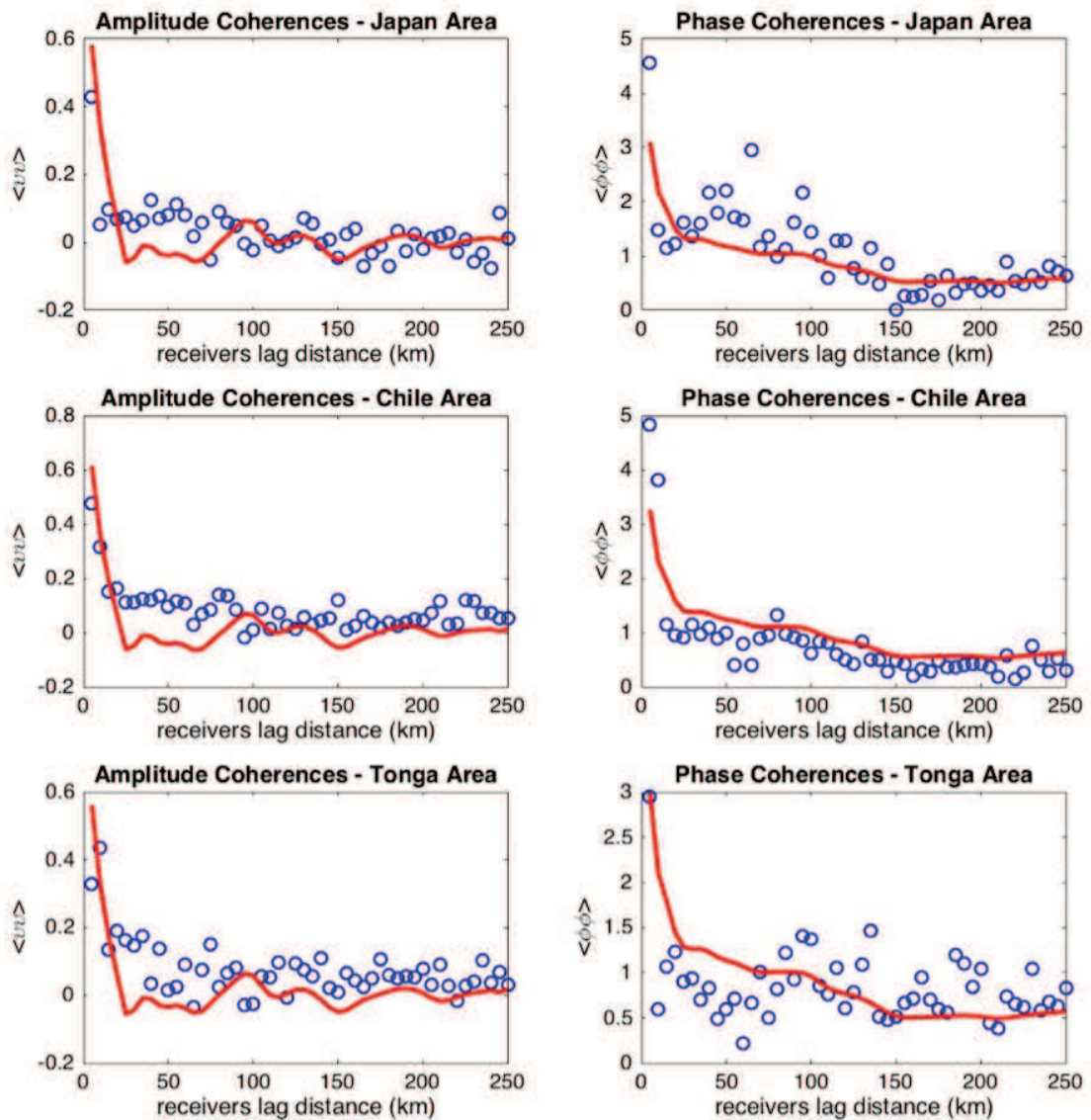


Figure 6: Comparison: Coherence functions (solid red line) calculated from the inverted heterogeneity spectrum of Fig. 5 compared with observed coherences (blue outlined circles).

where  $J_{PX}$  is the Jacobian of the function  $P$  with respect to parameter  $X$ . The inversion result is that  $a_g = 28, N = -0.4, \sigma = 0.9$ ;  $a_v$  becomes extremely large as the gradient descent iteration continues, so we set  $a_v = 2000$  to the physical reasonable limit: 2000 km as the scale invariance up-limit length [29]. A comparison of the best fit to observed coherence functions predicted from the inverted power spectrum is shown in Fig. 7.

For this model, R-squared is 0.52 and the reduced chi-squared is 1.71. Note although

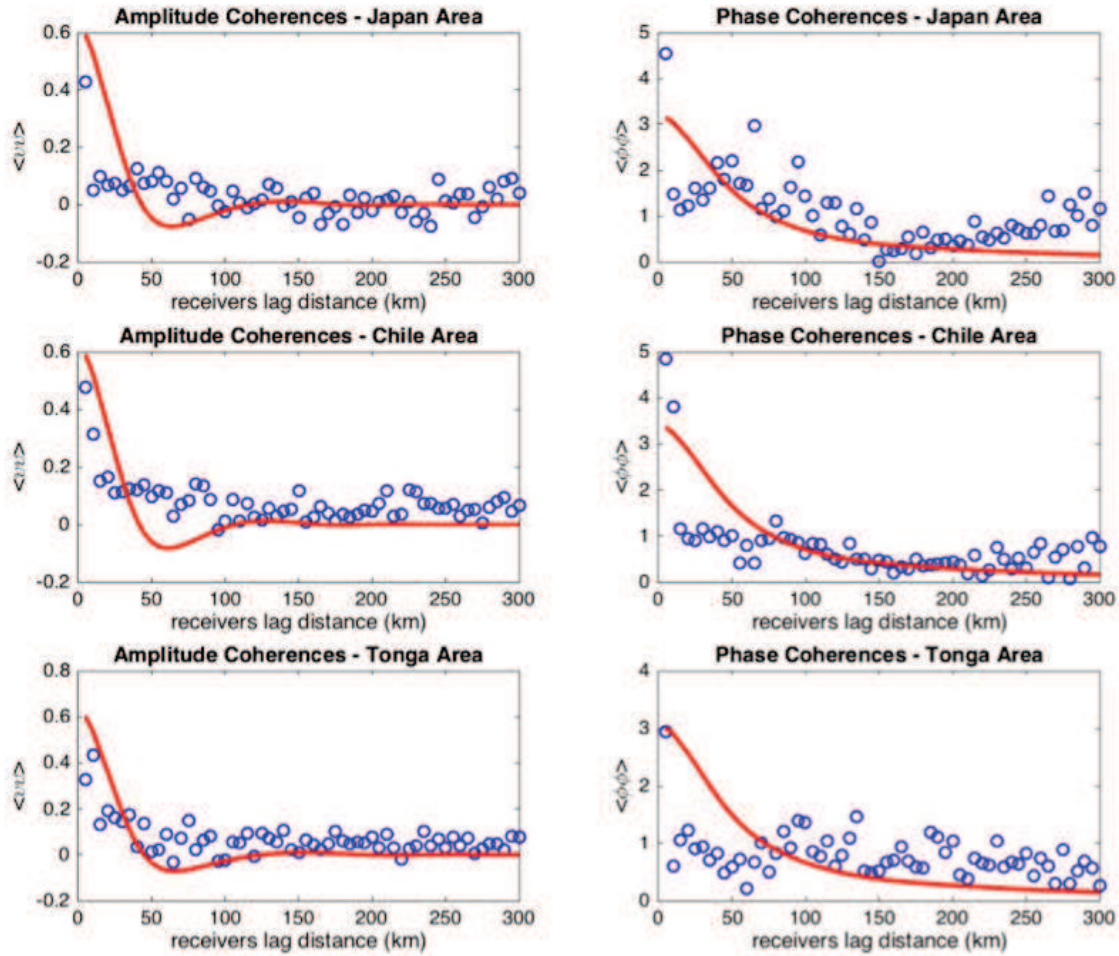


Figure 7: Comparison: Coherence functions (solid red line) calculated from the inverted heterogeneity spectrum regularized by the Klimes parameterization compared with observed coherences (blue outlined circles).

the prediction is not as good a fit, with a significant smaller coefficient of determination, the chi-square per degree of freedom is very similar to the previous inversion using Tikhonov regularization with more parameters. This suggests the Klimes function is still a good representation of the shape of the heterogeneity spectrum in wavenumber because it uses many fewer parameters (only four).

### 4.3 Inversion adding depth dependence

All traditional global tomographic studies resolve a strong depth dependence to the heterogeneity spectrum in the upper mantle, e.g., Ref. [30]. The fitting of TCFs from a combination of three epicentral regions in the inversion should intrinsically have strong sen-

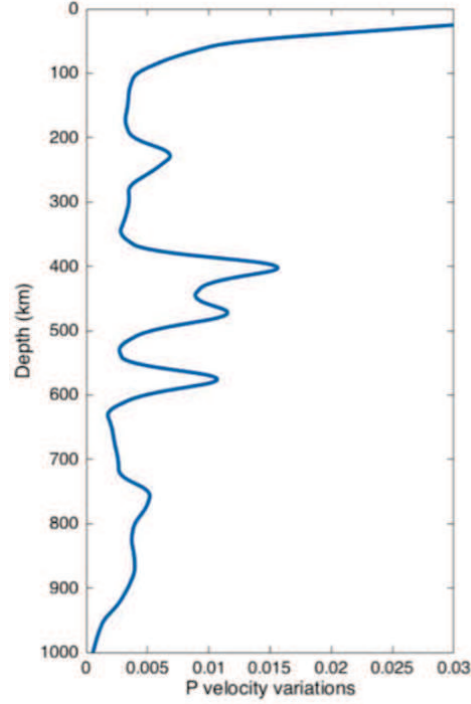


Figure 8: P velocity variations from the inverted power spectrum assuming depth dependency.

sitivity to this depth dependence due to the effects of crossing ray-paths similar to those illustrated for ACF and JCTAF in Figs. 1b and 1c. Recognizing this, we next added a depth dependency to see if we could achieve a better fit to the measured coherence measurements. We let

$$P(k,z) = \sigma^2(z) P(k). \quad (4.7)$$

$P(k)$  is the inversion result obtained for the assumption of a single layer and  $\sigma(z)$  becomes the new inversion target function.  $\sigma$  is a measure of standard deviation of the P velocities. In this case the gradient descent iteration becomes:

$$\sigma_{new} = \sigma_{old} - 2\gamma \left( M_t^T (M_t (\sigma_{old}^2 P_k) - C_{ij}) \right)^T \sigma_{old} P_k. \quad (4.8)$$

The inversion result is shown in Fig. 8. A comparison of the best fit to observed coherence functions predicted from the inverted power spectrum is shown in Fig. 9. Note in Fig. 9 that the fit to the observed coherence functions has improved considerably compared to that obtained with the assumption of depth-independent heterogeneity (Figs. 6 and 7). For this model, R-squared is 0.80 and the reduced chi-squared is 1.05. This improved result shows the data are well fit and the number of the pending parameters is properly chosen.

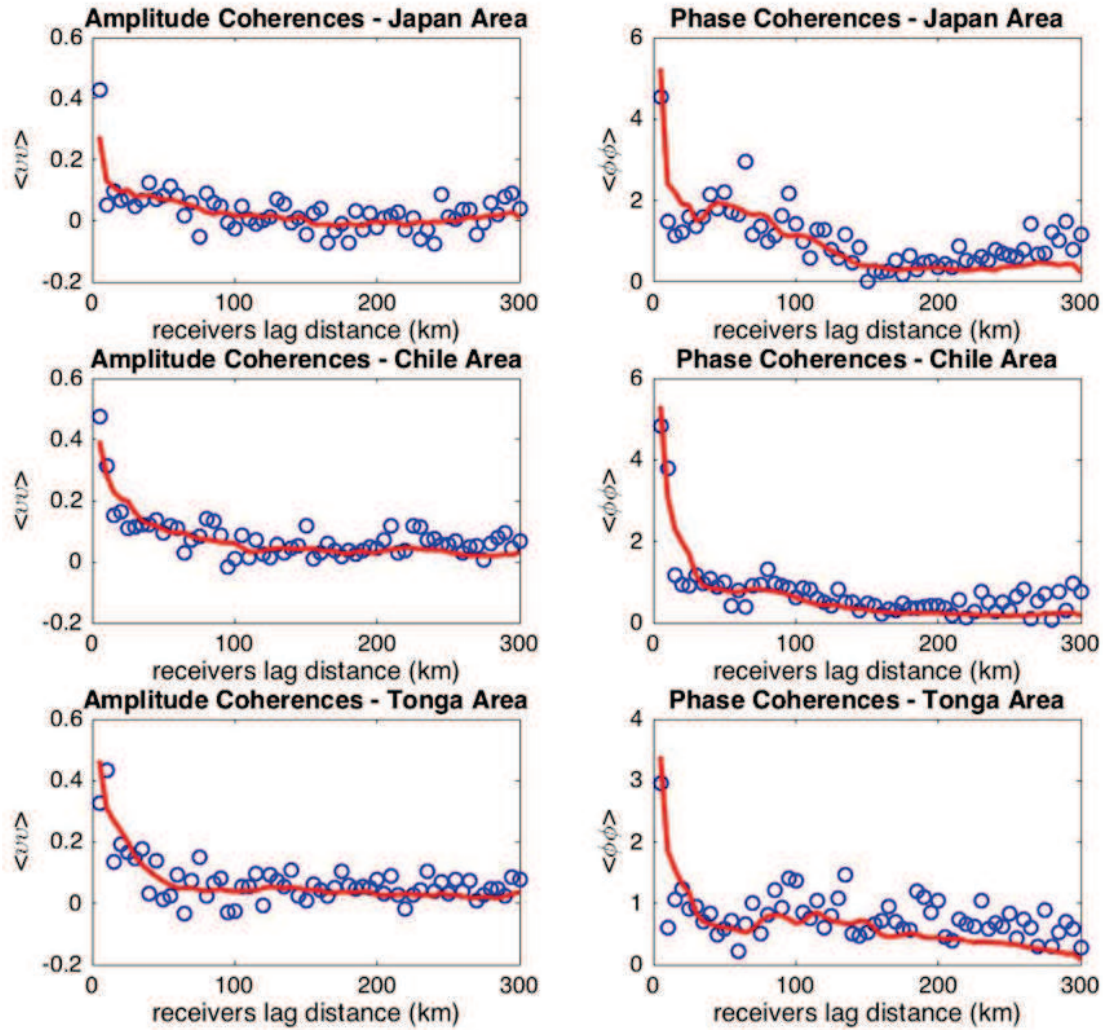


Figure 9: Comparison: Coherence functions (solid red line) calculated from the inverted heterogeneity spectrum assuming depth dependence with observed coherences (blue outlined circles).

## 5 Discussion and conclusions

### 5.1 Results assuming a single layer approximation

Figs. 5 and 6 show the inversion results with only L-2 regularization, from which we conclude:

- 1. Large power coefficient at low wavenumbers ( $< 0.018 \text{ km}^{-1}$ ) suggests that significant heterogeneity power exists in the upper mantle at large-scale ( $> 350 \text{ km}$ ).
- 2. A power peak at  $0.022 \text{ km}^{-1}$  suggests the existence of an important characteristic

length scale of 280 km. We can also see ripples between 0.058 km<sup>-1</sup> and 0.11 km<sup>-1</sup>, representing smaller heterogeneity peaking at 60 km to 100 km scale length.

- 3. The power decays with increasing wave number. For wavenumber larger than 0.12 km<sup>-1</sup>, the power coefficient tends to zero. The inverted power spectrum for a at least depth-independent model of upper mantle heterogeneity is approximately shaped like a low pass spatial filter.

Fig. 7 shows the result of the regularized Eq. (4.2). These inverted parameters are  $a_g = 28$ ,  $N = -0.4$ ,  $\sigma = 0.9$ ,  $a_v > 2000$ . The inner and outer cutoff scales of the self-affine random media [29] are the upper and lower limit for self-affine length scale:

$$a_g \ll x \ll a_v. \quad (5.1)$$

The result shows that upper mantle structure may be self-affine to even larger scale (hundreds of kilometers). This agrees with studies of smaller scales revealed by well-logging data that find the Earth to be fractal [31–33]. The parameter  $a_g$  is Gaussian low pass filter's characteristic length scale. The result  $a_g = 28$  indicates that smaller heterogeneities (smaller than 28 km) are excluded in this generalized spectrum, which agrees with our inversion result in Fig. 5. Although these parameters have reasonable physical meanings, the calculated coherence functions, however, are under-fit in Fig. 7. This is may be because the spectrum is over regularized by the Klimes function, true spectrum being more complex in a broader band, and/or that the spectrum is depth dependent.

## 5.2 Results assuming depth dependency

### 5.2.1 Effects of discontinuity topography

The inverted depth dependent P-wave variance in Fig. 8 shows a rather interesting result. Notice there are velocity variance peaks at different depths, including at the transition zone boundaries near 400 km and 650 km. One possibility is that these large velocity variances are the result of topography of the solid-solid phase changes at the transition zone boundaries. The difference between a reference Earth model with no topography on the phase changes and a true Earth with topography on those boundaries would be equivalent to heterogeneity perturbations concentrated along the hills and valleys of the phase change topography.

The topography of the velocity discontinuities near 400 and 650 km have been shown to generate underside reflections of body waves that arrive as precursors to the body waves reflected once at the surface, SS and PP. The majority of these studies have resolved features having lateral scale lengths on the order of 1000 km and greater, e.g., Ref. [34]. The maximum estimated perturbations to phase change depths approach 50 km, consistent with estimated temperature differences on the order of 50° to 300° K [35]. If temperature acted alone to affect the topography of phase changes, our coherence results suggest that significant lateral temperature differences exist in the mantle at significantly smaller scale (50 km to 350 km) than have been previously inferred from studies of

PP and SS precursors. From estimates of the thermal diffusivity of the upper mantle [36], the lower scale bound (50 km), is close to the limits of the plausible persistence of the this scale of observable temperature anomalies.

### 5.2.2 Effects of chemical and phase heterogeneity

An additional effect that can explain the peaks observed in the mantle heterogeneity spectrum is that of chemical heterogeneity, which can combine with the effects of lateral temperature heterogeneities. Stixrude and Lithgow-Bertelloni [37–39] have demonstrated that the temperature derivative of the velocity is a functional characterization of chemical and phase heterogeneity in the deep Earth. The isomorphous and metamorphic part is explained in a phase change diagram in Fig. 10, reproduced from their papers. The phases included are: orthopyroxene (opx), clinopyroxene (cpx), high-pressure Mg-rich clinopyroxene (hpcpx), garnet (gt), olivine (ol), wadsleyite (wa), ringwoodite (ri), perovskite (pv), CaSiO<sub>3</sub> perovskite (capv), and ferropericlase (fp), and stishovite (st). The metamorphic contribution to mantle heterogeneity is hard to recognize by the resolvable scale-lengths and effects of regularization in traditional deterministic tomography (Fig. 11).

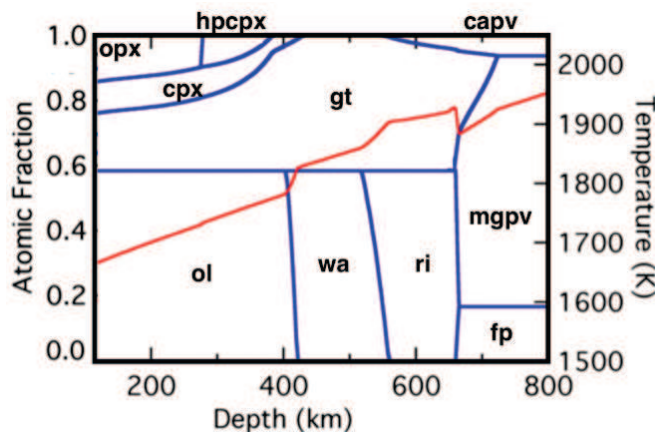


Figure 10: Calculated phase equilibrium [37-39]. Red line assumes an adiabatic temperature profile, which can be considered as the isomorphous contribution. Blue lines are complete phase equilibrium, which can be considered as metamorphic contribution.

If we compare our inversion to Stixrude and Lithgow-Bertelloni's predictions [39], from 100 km to 800 km, as in Fig. 12, we can see that the inverted spectra seem to capture the metamorphic contribution very well. This explains that velocity variance peaks in our inversion result are an effect of lithofacies metamorphosis. In this mechanism 3-D differences in temperature can move the heterogeneous collection of silicate minerals that comprise Earth's mantle into different regions of their phase diagrams, affecting the relative proportions of phases and their compositions, and hence their elastic velocities and densities.

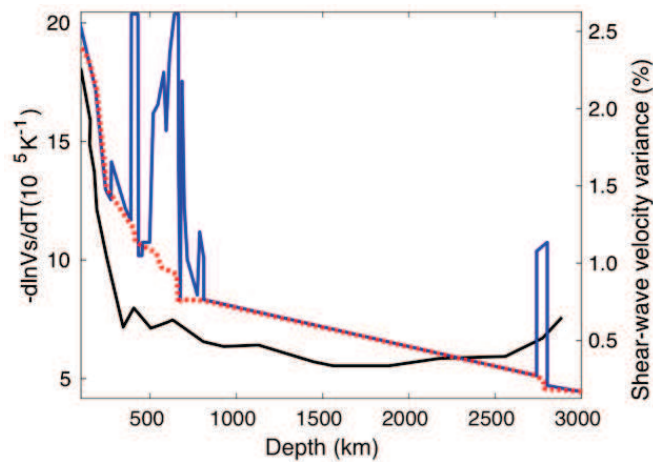


Figure 11: Temperature derivative of the shear wave velocity isomorph (red-dash) and metamorphic (blue-line), compared with example tomography model S20RTS (black-line) [39]. (Adapted from an original figure by Stixrude and Lithgow-Bertelloni [39].)

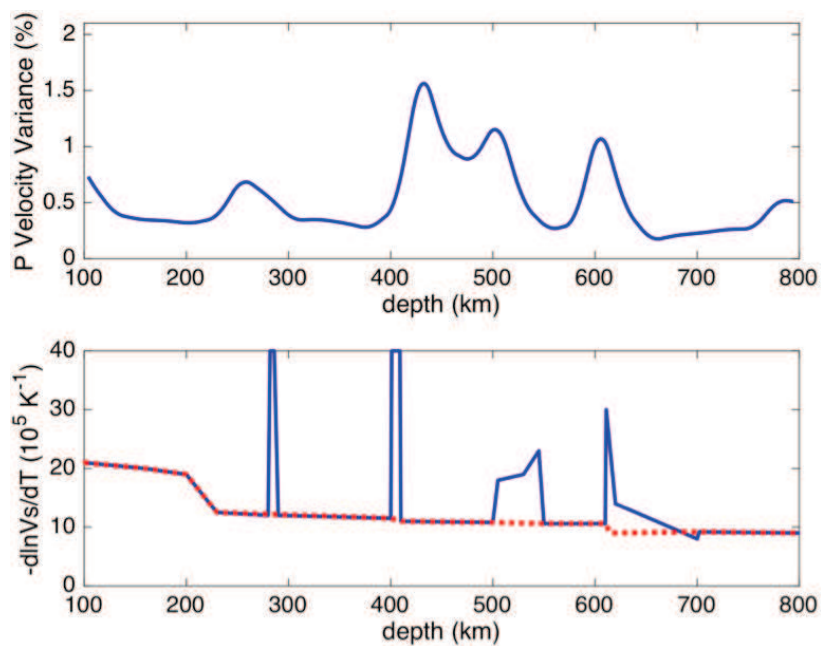


Figure 12: Inversion result for P velocity variance (upper) compared with the total temperature derivative of S wave velocity that incorporates effects of chemistry and phase [39].

Advances in computational seismology beginning in the 1970s, began to make it possible to identify phase changes near 400 km and 650 km from the analysis body waveform complexities due to triplications induced by sharp changes with depth in P and S veloci-

ties, e.g. [41]. The peaks in heterogeneity in Figs. 8 and 12 near 250 km and between 400 and 650 km, however, are not routinely identified from analyses of waveform complexity or reflected and converted body waves, suggesting that their associated phase and chemistry changes are spread out over depth intervals. The peak near 800 km in Figs. 8 and 12 may be a chemical signature of slab stagnation [42] at near that depth beneath western North America.

### 5.3 Summary results and future applications

In this work, we have demonstrated that stochastic tomography can be an important tool to understand the origin of mantle heterogeneity. The association of peaks in the depth variation of heterogeneity power with predicted solid-solid phase changes in known mantle silicates shows that lateral temperature and chemical variations act in concert with phase equilibria to produce significantly higher perturbations in elastic velocities than would be predicted from the temperature derivative of a mantle in a constant phase.

To achieve our results, we took care to eliminate the effects of source-side heterogeneity by the use of deep focus earthquakes and by averaging individual coherences measurements from clustered epicentral groups. Individual body wave measurements were also corrected for the source-time functions and radiation patterns. With these processing steps, applied to separate epicentral groups and large continental arrays, it may eventually be possible to employ stochastic tomography to verify or discover new solid-solid phase changes in the deep mantle.

## Acknowledgments

Vernon Cormier and Yiteng Tian were partially supported by grant EAR 14-46509 from the National Science Foundation (NSF), and Yingcai Zheng by NSF grant EAR 16-21878. This research was inspired by participation in a working group of the 2014 CIDER workshop.

## Appendices

### A Coherences predicted from specific heterogeneity spectra

#### A.1 Discretization

To calculate coherences from specific power spectra, we discretize the coherence functions given by Eq. (2.1) in Section 2 as follows:

$$\left. \begin{array}{l} \langle u_1 u_2 \rangle \\ \langle \phi_1 \phi_2 \rangle \\ \langle \phi_1 u_2 \rangle \end{array} \right\} = \text{IntegralMarix} \cdot P(h, k), \quad (\text{A.1})$$

where the Integral Matrix (I.M.) is

$$I.M. = \begin{cases} \frac{1}{2\pi} \sum_{i=1}^H dh \cdot a_{1i} \cdot a_{2i} \sum_{j=1}^K dk \cdot (j \cdot dk) \cdot \sin(\omega \vartheta_{1i,j}) \cdot \sin(\omega \vartheta_{2i,j}) \cdot J_0(j \cdot dk \cdot R_i), \\ \frac{1}{2\pi} \sum_{i=1}^H dh \cdot a_{1i} \cdot a_{2i} \sum_{j=1}^K dk \cdot (j \cdot dk) \cdot \cos(\omega \vartheta_{1i,j}) \cdot \cos(\omega \vartheta_{2i,j}) \cdot J_0(j \cdot dk \cdot R_i), \\ \frac{1}{2\pi} \sum_{i=1}^H dh \cdot a_{1i} \cdot a_{2i} \sum_{j=1}^K dk \cdot (j \cdot dk) \cdot \sin(\omega \vartheta_{1i,j}) \cdot \cos(\omega \vartheta_{2i,j}) \cdot J_0(j \cdot dk \cdot R_i). \end{cases} \quad (A.2)$$

Here  $dh$  and  $dk$  are numerical integral increments of depth and wave number. Subscript  $i$  denotes the iteration over depth and  $j$  denotes iteration over wavenumber. These functions  $a$  and  $R$  are only functions of depth, while  $\theta$  and Bessel term  $J_0(j \cdot dk \cdot R_i)$  are functions of both wave number and depth. Functions  $a_1$  and  $a_2$  are:

$$a_{1i} = \left(\frac{\omega}{c_i}\right) / \left(\omega \sqrt{\left(\frac{1}{c_i}\right)^2 - p_1^2}\right), \quad (A.3)$$

$$a_{2i} = \left(\frac{\omega}{c_i}\right) / \left(\omega \sqrt{\left(\frac{1}{c_i}\right)^2 - p_2^2}\right).$$

The  $\tau$  function (pre-calculated for all ray parameter  $p$ , with increment and its first derivative are discretized as

$$\tau_i(p) = \sum_{ii=1}^i dh \cdot \sqrt{\frac{1}{c_{ii}^2} - p^2}, \quad (A.4)$$

$$\tau'_i(p) = \frac{[\tau_i(p+dp) - \tau_i(p)]}{dp}. \quad (A.5)$$

Functions  $\vartheta_1$  and  $\vartheta_2$  are:

$$\vartheta_{1i,j} = \frac{1}{2} \cdot \left. \frac{[\tau'_i(p+dp) - \tau'_i(p)]}{dp} \right|_{p=p_2} \cdot \frac{(j \cdot dk)^2}{\omega^2},$$

$$\vartheta_{2i,j} = \frac{1}{2} \cdot \left. \frac{[\tau'_i(p+dp) - \tau'_i(p)]}{dp} \right|_{p=p_2} \cdot \frac{(j \cdot dk)^2}{\omega^2}. \quad (A.6)$$

Function  $R$  is the horizontal distance (great circle distance) of the two rays at specific depth. As discussed in Section 2.1, is a function of  $r_1$ ,  $r_2$ ,  $p_1$ ,  $p_2$  and depth. If we do not consider the effect of azimuth (assuming zero azimuth), and with two given incident plane waves (fixed ray parameters),  $R$  only depends on the depth and the surface lag

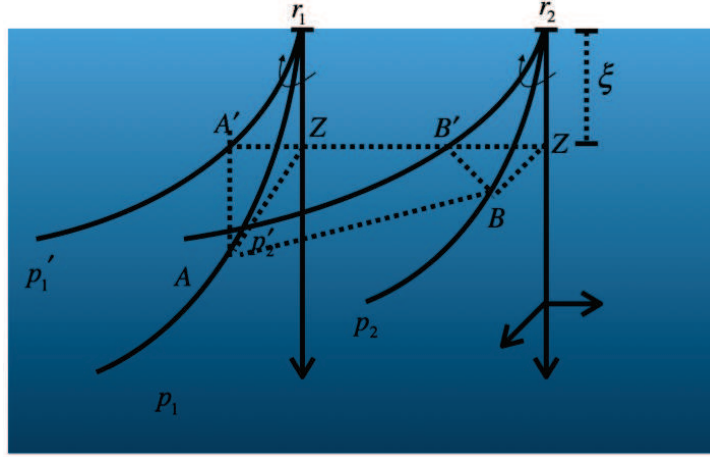


Figure 13: Geometry of two rays propagating to an array element.

distance between receivers. With the first derivative of  $\tau$  function (pre-calculated), we can easily compute  $R$  using following formula:

$$R_i = \text{abs} [lag - \tau'_i(p_1) + \tau'_i(p_2)]. \quad (\text{A.7})$$

If we take the azimuth into consideration, the calculation of  $R$  will differ. For the 3D case, as shown in Fig. 13,  $p_1$  and  $p_2$  are in different planes. We may rotate them to  $p_1'$  and  $p_2'$  so that the rays are in the same plane.

In this case, since  $ZA'$  is a rotation of  $ZA$ , these two length are both  $\tau'$ , as well as  $ZB$  and  $ZB'$ . If we take  $\Delta\varphi$  as the rotation angle's difference, then apply the cosine law to triangle  $\Delta ZBB'$  and  $\Delta ZAA'$ , we can easily have the following equation.

$$R = \sqrt{R'^2 + 4 \cdot \tau'_2 \cdot R' \cdot \sin^2\left(\frac{\Delta\varphi}{2}\right) + 4 \cdot \tau'_2{}^2 \cdot \sin^2\left(\frac{\Delta\varphi}{2}\right)}, \quad (\text{A.8})$$

where  $R'$  is a transform from Eq. (A.7),

$$R' = \text{abs} [lag + \tau'_1 - \tau'_2]. \quad (\text{A.9})$$

Although the formulas in Eq. (2.1) integrate  $\kappa$  from 0 to  $\infty$ , we set an upper limit to avoid under-sampling the integrand in regions of where it rapidly oscillates. For high wavenumber, the grid spacing should meet:

$$dk \leq \frac{4\pi\omega}{k\tau_{pp}}. \quad (\text{A.10})$$

In numerical tests, we found a stable and accurate integration is achieved by choosing the  $dk$  integration interval to be 0.001 km<sup>-1</sup> and the upper limit to be 0.3 km<sup>-1</sup>.

## B Inversion of coherence functions

Eq. (2.1) can be written as

$$C(\vec{x}) = M(\vec{x}, \vec{k}, z) \cdot P(\vec{k}, z), \quad (\text{B.1})$$

where  $C(\vec{x})$  are the measured coherence functions,  $M(\vec{x}, \vec{k}, z)$  is the discretized integral operator in Eq. (A.1);  $P(\vec{k}, z)$  is the 2.5-d power spectrum density function with respect to depth and wavenumber. With an axisymmetric approximation, this can be considered as the layered anisotropic power spectrum at each depth.

Using the measured coherence functions, we can solve for the power spectrum of the heterogeneity by minimizing

$$\left\| M(\vec{x}, \vec{k}, z) \cdot P(\vec{k}, z) - C(\vec{x}) \right\|. \quad (\text{B.2})$$

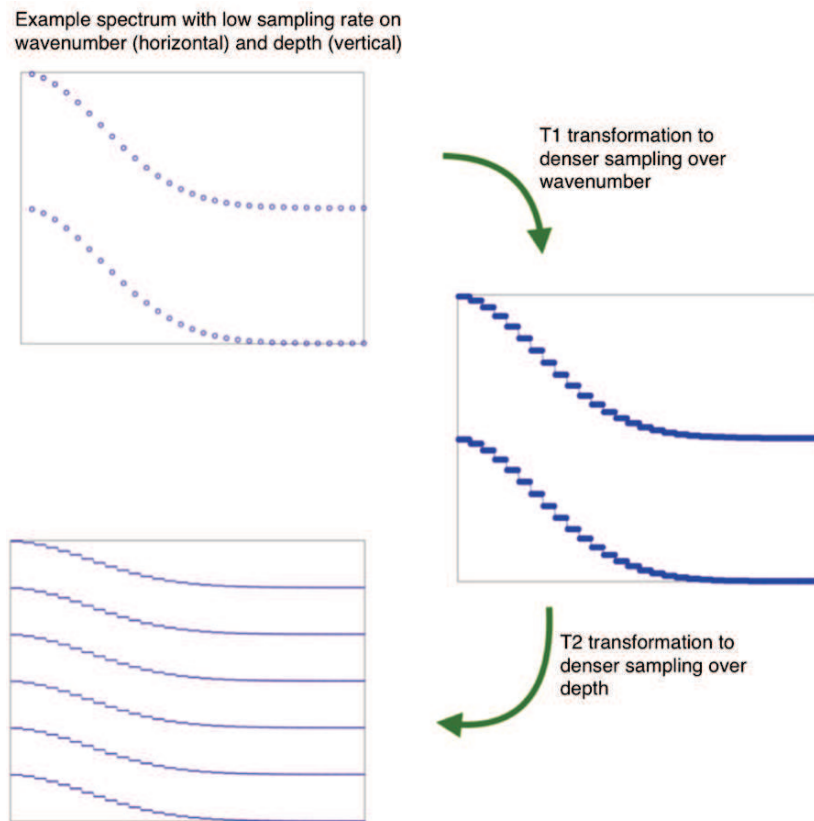


Figure 14: Transformation  $T1$  and  $T2$  in Eq. (B.5) as an up-sampling mapping, which is used to satisfy the limitation Eq. (A.10).

As discussed in Appendix A, the integral operator  $M$  can be discretized as an integral matrix. Then the equation becomes

$$C_{ij} = M_{ijmn} P_{mn}, \quad (\text{B.3})$$

where  $M_{ijmn}$  is the integral matrix in Eq. (A.2), with a dimension of  $(ij \times mn)$ , where  $i$  and  $j$  are the iterations over different discrete receivers,  $m$  and  $n$  are discrete intervals of depth and wave number respectively.  $i$  and  $j$  can be reduced to one variable or expanded to more variables depending on the calculation of either the transverse coherence functions (TCFs), or angular coherence functions (ACFs) or both.

We need to consider, however, the integral stability limitation, as discussed in Appendix A. If we let the grid spacing be small enough to satisfy this limitation,  $P(\vec{k}, z)$  may become a function with more unknown parameters than  $C(\vec{x})$ , making this inversion an under-determined problem. We may perform a linear transform to deal with this issue. Assuming the operator  $M$ , we calculate the integral over wave number first, then the integral over depth. The transform will then be

$$P_{m'n'} = T_1 T_2 P_{mn}, \quad (\text{B.4})$$

$$T_1|_{m' \times mn} = \begin{bmatrix} m' / m \begin{cases} 1 & 0 & \dots & 0 \\ 1 & 0 & \dots & 0 \\ \vdots & \vdots & \ddots & \vdots \\ 1 & 0 & \dots & 0 \end{cases} \\ \\ m' / m \begin{cases} 0 & 1 & \dots & 0 \\ 0 & 1 & \dots & 0 \\ \vdots & \vdots & \ddots & \vdots \\ 0 & 1 & \dots & 0 \end{cases} \\ \\ \vdots \\ \\ m' / m \begin{cases} 0 & 0 & \dots & 1 \\ 0 & 0 & \dots & 1 \\ \vdots & \vdots & \ddots & \vdots \\ 0 & 0 & \dots & 1 \end{cases} \end{bmatrix}, \quad T_2|_{m'n' \times m'} = \begin{bmatrix} m' \begin{cases} 1 & 0 & \dots & 0 \\ 0 & 1 & \dots & 0 \\ \vdots & \vdots & \ddots & \vdots \\ 0 & 0 & \dots & 1 \end{cases} \\ \\ m' \begin{cases} 1 & 0 & \dots & 0 \\ 0 & 1 & \dots & 0 \\ \vdots & \vdots & \ddots & \vdots \\ 0 & 0 & \dots & 1 \end{cases} \\ \\ \vdots \\ \\ m' \begin{cases} 1 & 0 & \dots & 0 \\ 0 & 1 & \dots & 0 \\ \vdots & \vdots & \ddots & \vdots \\ 0 & 0 & \dots & 1 \end{cases} \end{bmatrix}. \quad (\text{B.5})$$

$P_{m' \times n'}$  is the transformed target spectrum function and is the real target spectrum function with fewer parameters. The matrices of  $T_1$  and  $T_2$  actually work as an up-sampling transform, which is illustrated in Fig. 14.

If we let  $M_t = M_{ijmn} T_1 T_2$ , the object function then becomes

$$\min \|M_t P_{mn} - C_{ij}\|^2. \quad (\text{B.6})$$

The most straightforward way to do the inversion is to use a Moore Penrose inverse

$$P = M_t^T (M_t M_t^T)^{-1} C. \quad (\text{B.7})$$

Or a more computationally efficient way, a apply gradient descent method, by iterating

$$P_{new} = P_{old} - \gamma \cdot \nabla \|M_t P_{old} - C\|. \quad (\text{B.8})$$

Since the direct inversion is hard to regularize, we may invert the coherence functions step by step: first assuming a single layer spectrum, then add depth dependence.

## References

- [1] J.S. Buehler, P.M. Shearer, Pn tomography of the western United States using USArray, *Journal of Geophysical Research - Solid Earth*, 115 (2010).
- [2] K. Aki, Scattering of P waves under the Montana Lasa, *J. Geophys. Res.*, 78 (1973) 1334-1346.
- [3] S.M. Flatté, R.S. Wu, Small-scale structure in the lithosphere and asthenosphere deduced from arrival time and amplitude fluctuations at NORSAR, *J. Geophys. Res.*, 93 (1988) 6601-6614.
- [4] R.S. Wu, S.M. Flatté, Transmission fluctuations across an array and heterogeneities in the crust and upper mantle, *Pure Appl. Geophys.*, 132 (1990) 175-196.
- [5] X. Chen, K. Aki, General coherence functions for amplitude and phase fluctuations in a randomly heterogeneous medium, *Geophys. J. Int.*, 105 (1991) 155-162.
- [6] R.S. Wu, X. Xie, Numerical tests of stochastic tomography, *Phys. Earth Planet. Inter.*, 67 (1991) 180-193.
- [7] Y. Zheng, R.S. Wu, Theory of Transmission Fluctuations in Random Media with a Depth-Dependent Background Velocity Structure, in: *Advances in Geophysics*, 2008, pp. 21-41.
- [8] Y. Zheng, R.S. Wu, Measurement of phase fluctuations for transmitted waves in random media, *Geophysical Research Letters*, 32 (2005).
- [9] R.S. Wu, X. Xie, Y. Zheng, Amplitude and phase fluctuations of seismic waves and characterization of small-scale heterogeneities in the earth., *The Journal of the Acoustical Society of America*, 4 (2009).
- [10] R. Detrick, R. Woodward, J. Taber, T. Ahern, *Seismological Facilities for the Advancement of Geoscience and EarthScope*, in, NSF-EAR-Division Of Earth Sciences, 2013.
- [11] A.M. Dziewonski, T.-A. Chou, J.H. Woodhouse, Determination of earthquake source parameters from waveform data for studies of global and regional seismicity, *J. Geophys. Res. Lett.*, 86 (1981) 2825-2852.
- [12] Y. Zheng, Scale lengths of heterogeneities under Tibet, *Earthquake Science*, 26 (2013) 409-414.
- [13] D.H. Johnson, D.E. Dudgeon, *Array Signal Processing: Concepts and Techniques*, Prentice-Hall, 1993.
- [14] S. Burdick, F.L. Vernon, V. Martynov, J. Eakins, T. Cox, J. Tytell, T. Mulder, M.C. White, L. Astiz, G.L. Pavlis, R.D. van der Hilst, upper-mantle heterogeneity beneath North America from travel-time tomography with global and US Array data, *Seismol. Res. Lett.*, 88 (2017).
- [15] T. Nissen-Meyer, M. van Driel, S.C. Sthler, K. Hosseini, S. Hempel, L. Auer, A. Colombi, A. Fournier, AxiSEM: broadband 3-D seismic wavefields in axisymmetric media, *Solid Earth*, 5 (2014) 425-445.

- [16] L. Krischer, A. Hutko, M. van Driel, S. Sthler, M. Bahavar, C. Trabant, T. Nissen-Meyer, On-demand custom broadband synthetic seismograms, *Seismol. Res. Lett.*, 88 (2017).
- [17] M. van Driel, L. Krischer, S.C. Sthler, K. Hosseini, T. Nissen-Meyer, Instaseis: instant global seismograms based on a broadband waveform database, *Solid Earth*, 6 (2015) 701-717.
- [18] B.L.N. Kennett, *IASPEI 1991 Seismological Tables*, Bibliotech, (1991) 167.
- [19] G. Ekstrm, M. Nettles, A.M. Dziewoski, The global CMT project 2004-2010: Centroid-moment tensors for 13,017 earthquakes, *Physics of the Earth and Planetary Interiors*, 200-201 (2012) 1-9.
- [20] D.B. Percival, A.T. Walden, *Spectral Analysis for Physical Applications: Multitaper and Conventional Univariate Techniques*, Cambridge University Press, Cambridge, UK, 1993.
- [21] D.J. Thomson, Spectrum estimation and harmonic analysis, *Proceedings of the IEEE*, 70 (1982) 1055-1096.
- [22] J.C. VanDecar, R.S. Crosson, Determination of teleseismic relative phase arrival times using multi-channel cross-correlation and least squares, *Bulletin of the Seismological Society of America*, 80 (1990) 150-169.
- [23] W.L. Rodi, S.C. Myers, Computation of travel-time covariances based on stochastic models of velocity heterogeneity, *Geophys. J. Int.*, 194 (2013).
- [24] E. Hopper, K.M. Fischer, The changing face of the lithosphere-asthenosphere boundary: imaging continental scale patterns in upper mantle structure across the contiguous U.S. with Sp converted waves, *G-cubed*, (2018).
- [25] A.N. Tikhonov, V.Y. Arsenin, *Solution of Ill-posed Problems*, Winston and Sons, Washington, 1977.
- [26] K. Klimes, Correlation Functions of Random Media, *Pure appl. geophys.*, 159 (2002) 1811-1831.
- [27] P.S. Addison, *Fractals and Chaos: An Illustrated Course*, IOP Publishing, London, 1997.
- [28] D.L. Turcotte, *Fractals in Geology and Geophysics*, *Pure Appl. Geophys.*, 131 (1989) 171-196.
- [29] B.B. Mandelbrot, *The Fractal Geometry of Nature*, W.H. Freeman and Co., New York, 1977.
- [30] Y.J. Gu, A.M. Dziewoski, W. Su, G. Ekstrom, Models of the mantle shear velocity and discontinuities in the pattern of lateral heterogeneities, *J. Geophys. Res.*, 106 (2001).
- [31] R.S. Wu, X. X., L.X. P., Heterogeneity spectrum and scale-anisotropy in the upper crust revealed by the German Continental Deep-Drilling (KTB) holes, *Geophys. Res. Lett.*, 21 (1994) 911- 914.
- [32] A.G. Jones, K. Holliger, Spectral analyses of the KTB sonic and density logs using robust nonparametric methods, *J. Geophys. Res.*, 102 (1997) 18391-18403.
- [33] J.A. Goff, K. Holliger, Nature and origin of upper crustal seismic velocity fluctuations and associated scaling properties; combined stochastic analyses of KTB velocity and lithology logs, *J. Geophys. Res.*, 104 (1999) 13169-13182.
- [34] C. Houser, G. Masters, M. Flanagan, and P. Shearer, Determination and analysis of long-wavelength transition zone structure using SS precursors, *Geophys. J. Int.*, 174 (2008), 178-194.
- [35] M. Saki, C. Thomas, S.E.J. Nippers, and S. Lessing, Topography of upper mantle seismic discontinuities beneath the North Atlantic: The Azores, Canary and Cape Verde plumes, *Earth Planet. Sri. Lets.*, 409 (2015), 193-202.
- [36] B. Gibert, U. Seipold, A. Tommasi, and D. Mainprice, Thermal diffusivity of upper mantle rocks: Influence of temperature, pressure, and doformation fabric, *J. Geophys. Res.*, 108 (2003), doi: 10.1029/2002JB002108.
- [37] J. Ita, L. Stixrude, Petrology, elasticity, and composition of the mantle transition zone., *J.*

- Geophys. Res., 97 (1992).
- [38] L. Stixrude, C. Lithgow-Bertelloni, Influence of phase transformations on lateral heterogeneity and dynamics in Earth's mantle, *Earth and Planetary Science Letters*, 263 (2007) 45-55.
  - [39] L. Stixrude, C. Lithgow-Bertelloni, Geophysics of Chemical Heterogeneity in the Mantle, *Annual Review of Earth and Planetary Sciences*, 40 (2012) 569-595.
  - [40] J. Ritsema, H. van Heijst, J.H. Woodhouse, Global transition zone tomography, *J. Geophys. Res.*, 109 (2004).
  - [41] D.V. Helmberger and L.J. Burdick, Synthetic seismograms, *Ann. Rev. Earth Planet. Sci.* 7 (1979), 417-442.
  - [42] M.D. Ballmer, N.C. Schmerr, T. Nakagawa, J. Ritsema, Compositional mantle layering revealed by slab stagnation at  $\sim 1000$ -km depth, *Sci. Adv.* 1(11), (2015), doi: 10.1125/sciadv.1500815.